MICROELECTRONICS RELIABILITY

Clay Mayberry and Joseph Bernstein

17 Jan 2017

Interim Report

APPROVED FOR PUBLIC RELEASE; DISTRIBUTION IS UNLIMITED.

AIR FORCE RESEARCH LABORATORY
Space Vehicles Directorate
3550 Aberdeen Ave SE
AIR FORCE MATERIEL COMMAND
KIRTLAND AIR FORCE BASE, NM 87117-5776

DTIC COPY
NOTICE AND SIGNATURE PAGE

AFRL-RV-PS-TR-2016-0155 HAS BEEN REVIEWED AND IS APPROVED FOR PUBLICATION IN ACCORDANCE WITH ASSIGNED DISTRIBUTION STATEMENT.

//SIGNED//   //SIGNED//
CLAY MAYBERRY   DAVID CARDIMONA
Program Manager   Technical Advisor, Space Based Advanced Sensing
                                                          and Protection

//SIGNED//
JOHN BEAUCHEMIN
Chief Engineer, Spacecraft Technology Division
Space Vehicles Directorate

REPORT DOCUMENTATION PAGE

Form Approved
OMB No. 0704-0188

Public reporting burden for this collection of information is estimated to average 1 hour per response, including the time for reviewing instructions, searching existing data sources, gathering and maintaining the data needed, and completing and reviewing this collection of information. Send comments regarding this burden estimate or any other aspect of this collection of information, including suggestions for reducing this burden to Department of Defense, Washington Headquarters Services, Directorate for Information Operations and Reports (0704-0188), 1215 Jefferson Davis Highway, Suite 1204, Arlington, VA 22202-4302. Respondents should be aware that notwithstanding any other provision of law, no person shall be subject to any penalty for failing to comply with a collection of information if it does not display a currently valid OMB control number. **PLEASE DO NOT RETURN YOUR FORM TO THE ABOVE ADDRESS.**

1. REPORT DATE *(DD-MM-YYYY)*	2. REPORT TYPE	3. DATES COVERED *(From - To)*
17-01-2017	Interim Report	1 Jan 2015-1 Jan 2017

4. TITLE AND SUBTITLE

Microelectronics Reliability

5a. CONTRACT NUMBER

5b. GRANT NUMBER

5c. PROGRAM ELEMENT NUMBER
62601F

6. AUTHOR(S)

Clay Mayberry and Joseph Bernstein

5d. PROJECT NUMBER
4846

5e. TASK NUMBER
PPM00015032

5f. WORK UNIT NUMBER
EF126566

7. PERFORMING ORGANIZATION NAME(S) AND ADDRESS(ES)
Air Force Research Laboratory
Space Vehicles Directorate
3550 Aberdeen Ave SE
Kirtland AFB, NM 87117-5776

8. PERFORMING ORGANIZATION REPORT NUMBER

AFRL-RV-PS-TR-2016-0155

9. SPONSORING / MONITORING AGENCY NAME(S) AND ADDRESS(ES)

10. SPONSOR/MONITOR'S ACRONYM(S)
AFRL/RVSW

11. SPONSOR/MONITOR'S REPORT NUMBER(S)

12. DISTRIBUTION / AVAILABILITY STATEMENT
Approved for public release; distribution is unlimited. (OPS-17-12864, 17 Jan 17)

13. SUPPLEMENTARY NOTES

14. ABSTRACT
In this research, an innovative and practical way to use the various physics of failure equations is shown together with accelerated testing for reliability prediction of devices exhibiting multiple failure mechanisms. Also presented was an integrated accelerating and measuring platform to be implemented inside FPGA chips, making the MTOL testing more accurate, allowing these tests at the chip and perhaps at the system level, rather than only at the transistor level. The calibration of physics models with highly accelerated testing of complete commercial devices allows for actual reliability prediction. The MTOL Matrix can provide information about the proportional effect of each failure mechanism; allowing extrapolation of the expected reliability of the device under various conditions.

15. SUBJECT TERMS
Boltzmann-Arrhenius-Zhurkov, Multiple Temperature Overstress Life-test, Negative bias temperature instability, Physics of Failure, Deep submicron technology

16. SECURITY CLASSIFICATION OF:			17. LIMITATION OF ABSTRACT	18. NUMBER OF PAGES	19a. NAME OF RESPONSIBLE PERSON Clay Mayberry
a. REPORT Unclassified	**b. ABSTRACT** Unclassified	**c. THIS PAGE** Unclassified	Unlimited	30	**19b. TELEPHONE NUMBER** *(include area code)*

Standard Form 298 (Rev. 8-98)
Prescribed by ANSI Std. 239.18

--- This Page Intentionally Left Blank ---

TABLE OF CONTENTS

LIST OF FIGURES

LIST OF TABLES

1   SUMMARY

The Space Electronics Technology (SET) Branch has recognized that micro-, and now nano-electronics reliability is an important area of research concomitant with advanced electronics technology development that rely on extremely miniaturized devices. The branch historically has studied the role and dynamics of defects and charges in oxides and their effects on complementary metal oxide semiconductor (CMOS) circuits, the effect of negative and positive bias temperature instability (NBTI and PBTI) on CMOS and recommended mitigation schemes to counter these effects, experimentally measured the sensitivities of the high-k dielectric oxides incorporated into the gates of deep submicron devices with respect to ionizing radiation, and even delved into the reliability and effectiveness of organic photovoltaics in space environments at the request of Dr. Charles Lee of the Air Force Office of Scientific Research (AFOSR). The scope of the effort has included both modeling and experiments of both unexposed and exposed devices to ionizing radiation, in fact the goal of the ongoing effort was to study the synergistic effects of ionizing radiation on the NBTI degradation mechanism, of special interest to the Space Electronics Branch since NBTI was shown experimentally to be the limiting degradation mechanism to space based electronic systems utilizing CMOS, that include all processors and most memories. The focus of the effort was shifted from studying specific degradation mechanisms to developing an experimental reliability estimating methodology that could both illuminate the lifetime reliability of advanced devices, circuits and systems, and be incorporated into a space qualification methodology for advanced circuits and systems. The philosophy is to let other scientific groups with access to devices for testing and with a communication path with the foundries to allow them to alter fabrication and processing as necessary to incorporate recommended changes, our group will dedicate resources to developing and using an end of the line, experimentally based, reliability estimating tool. This interim report is dedicated towards explaining the development of the tool and the progress towards implementing it in the SET.

2 INTRODUCTION

The key innovation of the Multiple-Temperature Operational Life (MTOL) testing method is its success in separating different failure mechanisms in devices in such a way that actual reliability predictions can be made for any user defined operating conditions. This is opposed to the common approach for assessing device reliability today, using High Temperature Operating Life (HTOL) testing [1], which is based on the assumption that just one dominant failure mechanism is acting on the device [2]. However, it is known that multiple failure mechanisms act on the device simultaneously [3]. The new approach, MTOL, deals with this issue [4] (in that paper, it is called it M-HTOL). This method predicts the reliability of electronic components by combining the Failure in Time (FIT) of multiple failure mechanisms [5]. Degradation curves are generated for the components exposed to accelerated testing at several different temperatures and core stress voltages. The data clearly reveals that different failure mechanisms act on the components in different regimes of operation causing different mechanisms to dominate depending on the stress and the particular technology. A linear matrix solution, as presented in [5], allows the failure rate of each separate mechanism to be combined linearly to calculate the actual reliability as measured in FIT of the system based on the physics of degradation at specific operating conditions.

In this research, the experimental results of the MTOL method tested on both 45 and 28 nm field programmable gate array (FPGA) devices from Xilinx that were processed at Taiwan Semiconductor Manufacturing Company (TSMC) (according to the Xilinx data sheets) are presented. The FPGAs were tested over a range of voltages, temperature and frequencies. Ring frequencies of multiple asynchronous ring oscillators were measured simultaneously during stress in a single FPGA. Hundreds of oscillators and the corresponding frequency counters were burned into a single FPGA to allow monitoring of statistical information in real time. Since the frequency itself monitors the device

degradation, there is no recovery effect whatsoever, giving a true measure for the effects of all the failure mechanisms in real time.

The results produced an acceleration factor (AF) for each failure mechanism as a function of core voltage, temperature and frequency. The failure rates of all of the mechanisms were then combined using a matrix to normalize the AF of the mechanisms to find the overall Failure in Time or FIT of the device. In other words an accurate estimate of the device lifetime was found and thus the reliability that can be conveniently transposed to other technologies and application specific integrated circuits (ASICs) and not necessarily only FPGAs.

3   METHODS, ASSUMPTIONS AND PROCEDURES

3.1 MTOL Testing System

The FPGA configuration designed for the MTOL testing consists of three main parts: (1) Accelerated Element (FPGA Chip); (2) Measurement system (Binary Counter); (3) Control & communication interface to a personal computer (see Fig. 1). The test systems consisted of two development boards containing either a Xilinx XC6SLX9 Spartan 6 FPGA (45 nm) built on a Mojo® board or a Zynq-7000 FPGA (28 nm) built on a Zybo® board.
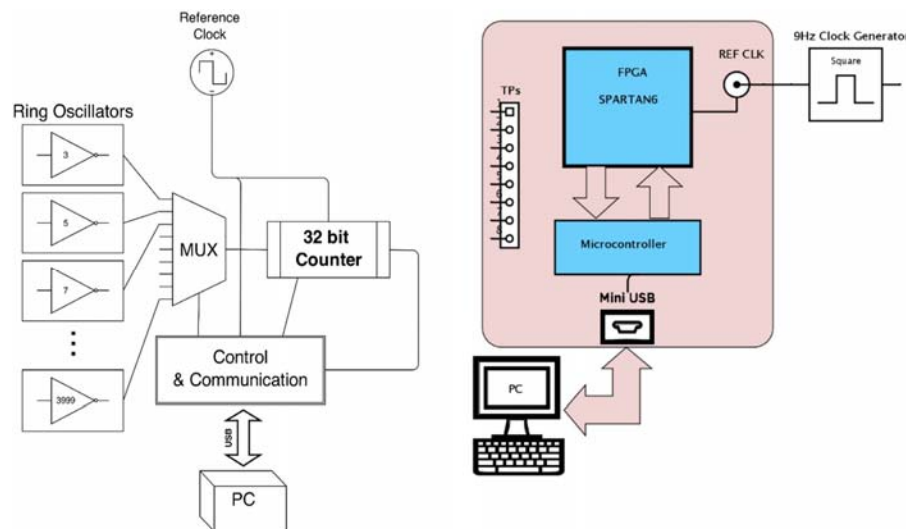

Figure 1 Testing setup consisting of ring oscillators, counter and communication.

The Spartan 6 uses TSMC's 45 nm low power process for 1.2 V core voltage and the Zynq-7000 FPGA is from high-K metal gate (HKMG) high performance low power process that is optimized for 1.0 V core voltage. The devices contain over 9000 logic cells, and the programs were designed to cover the full scope of the device's components. The devices included inputs for reference signals, testing points, and micro-USB interfaces.   In order to allow various voltage levels, an external DC power supply delivered voltage to the FPGA cores after overriding the internal voltage controls in the board.   The device temperature was monitored both internally and externally using an Infrared (IR) camera and internal temperature measurements.

3.2 The Accelerated Element

The accelerated element ran with several different frequencies, allowing independent measurements of the degradation effects over time as a function of frequency. In order to create a measurable accelerated system, Ring Oscillators (ROs) consisting of inverter chains were constructed (shown in Fig. 2). The frequency of each RO is given by: $1/2N\,T_p$, where N is the number of inverters and T_p is the time propagation delay per inverter. Each inverter chain was implemented as a complete logical cell using predefined Xilinx primitives and thus each ring oscillator was made up of the basic components of the FPGA.   When degradation occurred in the FPGA, a decrease in performance and frequency of the RO could be observed. For optimal testing and chip coverage, different sized ROs were selected, ranging from 3 inverters, giving the maximum frequency possible in accordance with the intrinsic delays of the FPGA employed (400–700 MHz), and up to 4001 inverter oscillators, giving a much lower frequency (around 200 KHz). The system implemented on the chip starts operating immediately when the FPGA core voltage is connected. This allows seeing the frequency dependence of the failure mechanisms without
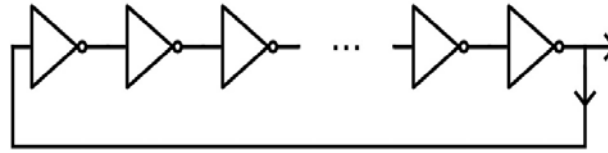
any recovery effect.

Figure 2 Ring oscillator is made of 2N + 1 inverters connected in a chain.

3.3 The Control System

The control system includes a programmable multiplexer (MUX), which switches between the various RO sampled outputs. Each cycle transfers a different RO for measurement and a communication controller that connects to a personal computer. The control system communicates with the computer via a USB connection with a simple serial protocol. The data received from the board is saved on a file in the computer in .csv format to be editable using a standard data processing program such as Excel.

3.4 The Counter

Frequency measurements were carried out from a crystal on the board. For high-resolution measurements, a 32-bit counter was chosen. Assuming the highest available frequencies to be around 700 MHz, a Reference Clock signal of 9 Hz was fed into the FPGA. The reference signal was generated outside of the FPGA (and the accelerated environment) allowing as accurate measurements as possible. The reference signal is also returned to the exterior in order to verify that the measurement remains accurate throughout the experiments.

3.5 Testing Methods

The test conditions, i.e. voltage and temperature levels were defined in a test plan for imposing an acceleration of individual mechanisms to dominate others at each applied condition. For example, testing in sub-zero temperatures and high voltages, will exaggerate Hot Carrier Injection (HCI) for high frequency [6] [7] but very low degradation due to Bias Temperature Instability (BTI) [8] .

For each test, the FPGA board was placed in a temperature controlled oven, similar to those used

in HTOL-testing, with an appropriate voltage connected at the FPGA core from an external supply. The board was connected to a computer via USB cables. The tests were performed for 100–200 h, while the device was operating at accelerated voltage conditions - the frequencies of 140 Ring-Oscillators of different sizes were sampled every 5 min [9]. The measured data was stored in a database from which one could draw statistical information about the degradation in the device performance.

The particular testing conditions were chosen to isolate each failure mechanism allowing examination of the specific effect of that mechanism on the system and thus define its unique physical characteristics. A close inspection of the results in comparison to one another yielded more precise parameters for the AF equations and allowed adjusting them to fit all the devices under test [10] .

Finally, after completing the tests, some of the experiments with different frequency, voltage and temperature conditions were chosen to construct the MTOL Matrix. The calculated FIT was then plotted as a function of temperature and frequency for every operating voltage. Since the FIT calculation is, in essence, an average of a large number of devices (10^7 transistors), we assume the Poisson model to postulate that the standard deviation is equal to the time to fail.

3.6 Separating Failure Mechanisms

The common intrinsic failure mechanisms affecting electronic devices are (HCI), (BTI), Electromigration (EM) and Time Dependent Dielectric Breakdown (TDDB). In our tests, no signature of TDDB was observed. This result is not surprising considering that in other accelerated test results on comparable technologies TDDB is only observed in voltages higher than 1.6 V [11] . The standard models for failure mechanisms in semiconductor devices are classified by JEDEC Solid State Technology Association and listed in publication JEP-122G [12]. The failure mechanisms can be separated due to the difference of physical nature of each individual mechanism.

3.7 E_a and γ Extrapolation

The tests for various mechanisms included exposing the core of the FPGA to accelerating voltages above nominal. 45 nm defines the nominal voltage at 1.2 V and for 28 nm, 1.0 V. The method of separating mechanisms allowed the evaluation of actual activation energies for the three failure mechanisms detailed above. The degradation was plotted in frequency and attributed it to one of the three failure mechanisms as will be explained further on.

The results of the experiments give both the activation energy (E_a) and stress factor as a percentage of burnout limits (γ) for the three mechanisms that were studied at temperatures ranging from − 50 to 150 °C. The Eyring model [13] is utilized here to describe FIT for all of the failure mechanisms. This model, using a simple constant rate (1-parameter) Poisson function, conserves strict linearity. Any additional terms would be nonlinear and invalidate the Matrix. This linear, constant failure rate, approximation is born out of the observation that the statistical variability across the chip converges to the constant rate, Poisson process, allowing the linear matrix calculations to hold. The specific constant failure rate of each failure mechanisms, calculated as FIT follows these formulae:

$$FIT_{HCI} = fV^{\gamma_{HCI}} e^{-\frac{E_A \alpha_{HCI}}{kT}} \tag{1}$$

$$FIT_{BTI} = fV^{\gamma_{BTI}} e^{-\frac{E_A \alpha_{BTI}}{kT}} \tag{2}$$

$$FIT_{EM} = fV^{\gamma_{EM}} e^{-\frac{E_A \alpha_{EM}}{kT}} \tag{3}$$

where f is the driving signal frequency, γ is the factor of loading characterizing the role of the level of stress, V is the applied voltage, E_A is the activation energy, k is Boltzman's constant, α is the degradation slope, and T is the absolute temperature. The degradation slope, α, is measured as the degradation from initial frequency as an exponential decay, approximated by taking the difference in frequency, divided by initial frequency over the time. In the experiments, it was found that when the decay

was dominated by BTI, the decay was proportional to the 4th root of time, while HCI and EM, being diffusion related mechanisms, have decay that is proportional to the square root of time [14], as seen in figure 3. This result is consistent with literature and with the JEDEC document that lists the failure mechanisms, JEP-122G [12].

For each oscillator, the ring frequency was measured and plotted against the square root of time in 45 nm devices. The slope, α, was then converted to a FIT for each test as determined by extrapolating the degradation slope to 10% degradation from its initial value, One FIT is defined as 1 failure in 10^9 part-hours [13]. Each set is plotted as an exponential decay dependent on the square root of time as shown by example in Figure 3. This slope is then used to find the time to fail as seen in the development of FIT below (4–7).
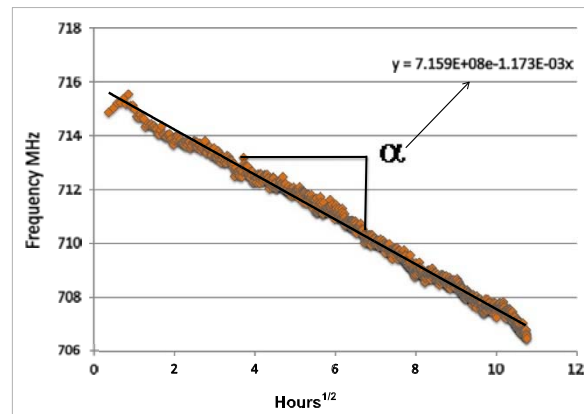

Figure 3 Typical graph showing frequency versus square root of time showing degradation slope, α.

$$\alpha_{(slope)} = \frac{\Delta f}{f_o \times \Delta\sqrt{t}} \tag{4}$$

$$TTF = \left(\frac{10\%}{\alpha}\right)^2 \tag{5}$$

$$FIT = \frac{10^9}{TTF} \tag{6}$$

$$FIT = 10^9(10 * \alpha)^2 \tag{7}$$

This makes our FIT easy to calculate, since FIT is defined as:

$$FIT = \frac{10^9}{MTTF} \tag{8}$$

Where MTTF is the mean time to fail in hours.

The time to fail for each point was then calculated as the square of the inverse slope times the failure criterion, which is 10% degradation [13]. Hence, the FIT for each slope is simply determined as the $(10*\alpha)2$. The average FIT is the metric to determine the reliability since that corresponds to the MTTF in Equation (8). This FIT value is plotted as a function of the frequency in order to determine the failure mechanisms and to fit the model parameters for each mechanism. Two typical degradation plots taken from 45 nm tests are shown in Figure 4, the FITs, determined by the slopes, are plotted against frequency in two different experiments. The data demonstrates the clear advantage of RO generated frequencies in a single chip [15]. In the examples of Fig. 4, it is shown that the HCI effect at a temperature of −20 °C and voltage of 2.0 V in 4a), showing FIT that is directly proportional to frequency [16], consistent with Equation (1). Figure 4b) shows a chip that was stressed at high voltage (2.4 V) and high temperature (150 °C) showing a strong BTI degradation at low frequency and a much shallower slope due to EM caused by an increase of effective resistance and therefore a frequency dependent effect [17] . Such curves were made for each experiment, incorporating all the oscillators across the chip spanning the range of frequencies, reflecting also the averaging effect of the longer chains. Hence, the variability is much lower than at higher frequencies, demonstrating that the averaging of many variations results in a consistent mean degradation. This strengthens credibility of modeling the failure mechanisms with equations (1–3) since the data shows a clear Poisson statistical nature. The slope of FIT versus frequency is then related at low temperatures as occurring only from HCI while at higher voltages and temperatures, it can be due to BTI [18] and EM. BTI is only responsible for low frequency degradation [19].
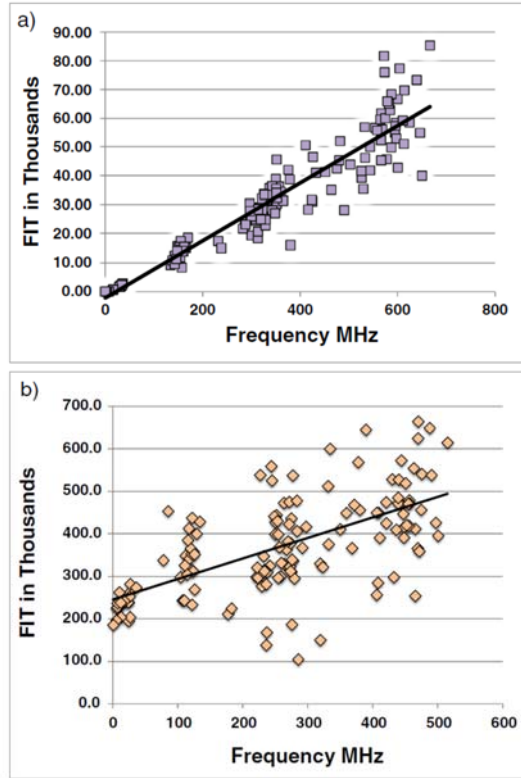
**Figure 4 Failure rate, FIT/1000, versus frequency in MHz
for a) HCI, stressed at −35 °C with 2.0 V core voltage and
b) BTI, stressed at 145 °C with 2.4 V at the core.**

In order to determine the dependence of each mechanism, the activation energy as relating to the temperature factor (T_F) and voltage acceleration factors (V_F) are determined from Equations (1 - 3). The result of FIT versus V, T and F are plotted as follows. HCI voltage constant γ was found by plotting FIT/TF versus V as seen in Figure 5a. Figure 5b shows the FIT/VF versus 1/kT looking only at temperatures below 5 °C in order to determine the activation energy, E_a. Since both plots depend on each other, the two are performed simultaneously, where Ea is used to determine TF, where:

Approved for public release; distribution is unlimited.
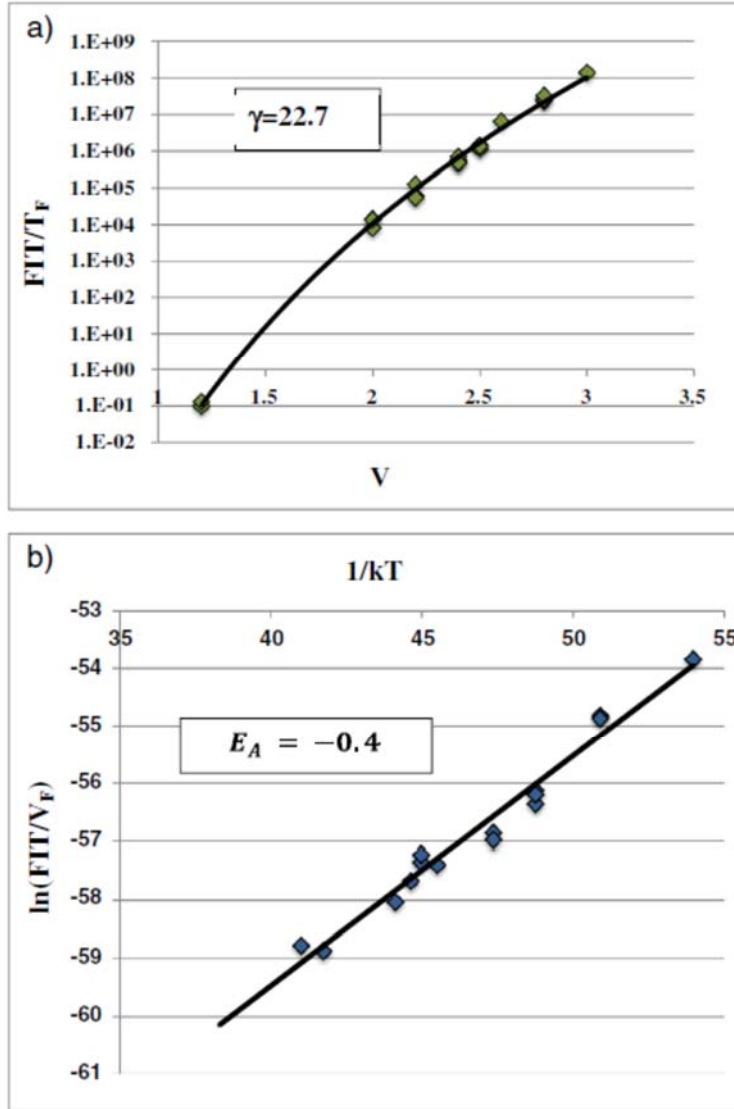
Figure 5 (a) Gamma plot for HCI at 45 nm, (b) Activation energy plot for HCI at 45 nm.

$$T_F = e^{\frac{-E_a}{kT}} \tag{9}$$

$V_F = V^\gamma$ for HCI and EM and $V_f = e^{\gamma V}$ for BTI $\tag{10}$

Hence, we were able to find the correct activation energy simultaneously with its corresponding

voltage factor. Our procedure was followed for all three mechanisms for the 45 nm as well as the 28 nm

devices. In the 28 nm device, there was no apparent effect from HCI or EM. That is to say that no slope was

found versus frequency. This is in contrast with the 45 nm devices, showing frequency related effects at both low temperatures due to HCI and a minor EM effect at high temperatures [20]. The E_a and γ for HCI are plotted in figures 5a and b as found in 45 nm. The plots for EM are shown in figure 6a and b while the BTI curves are shown in figure 7a and b for 45 nm devices and in figure 8a and b for the 28 nm BTI effect. The constants are summarized in Table 1.
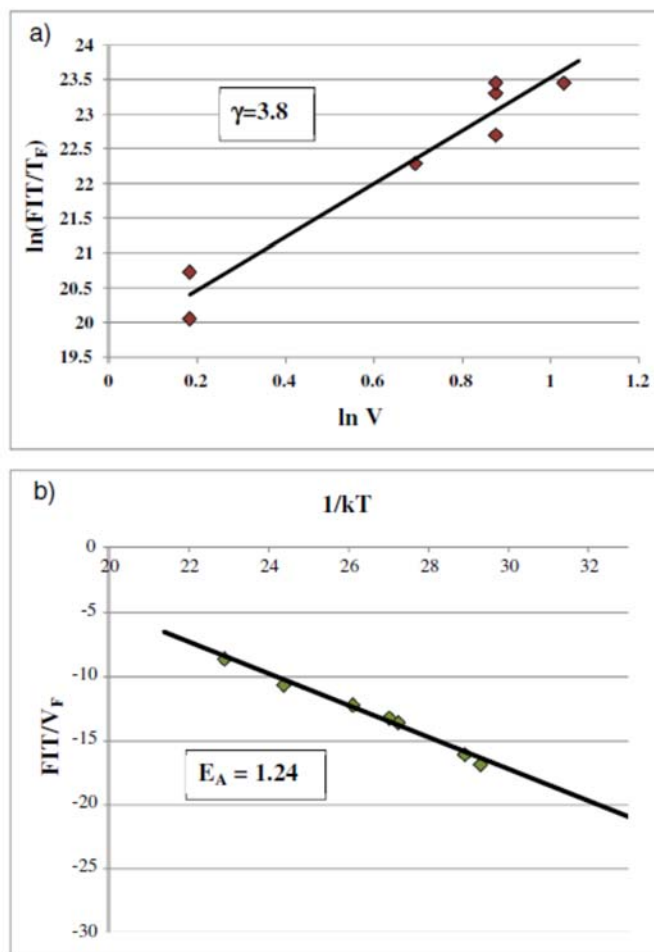
Figure 6 (a) Gamma plot for EM at 45 nm, (b) Activation energy plot for EM at 45 nm.

Table 1 Summary of E_A and ϒ from the curve fits.

	E_a 45 nm (eV)	γ 45 nm	E_a 28 nm (eV)	γ 28 nm
HCI	-0.4	22.7		
BTI	0.52	$3.8\ V^{-1}$	.52	$17.2\ V^{-1}$
EM	1.24	3.8		
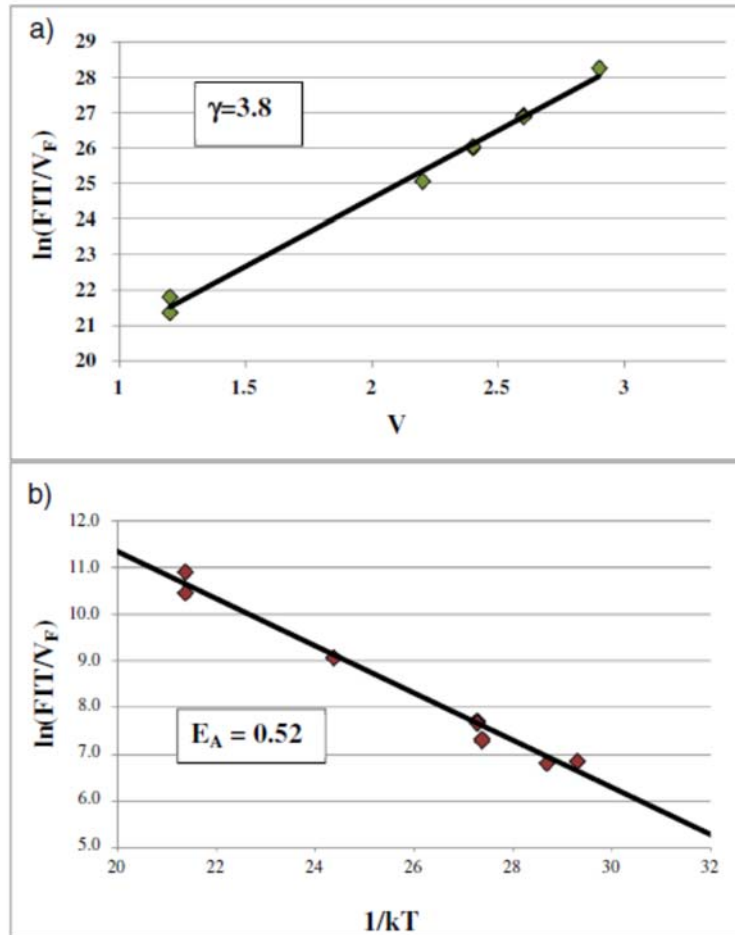
Figure 7 (a) Gamma plot for BTI at 45 nm, (b) Activation energy plot for BTI at 45 nm.

Approved for public release; distribution is unlimited.

13
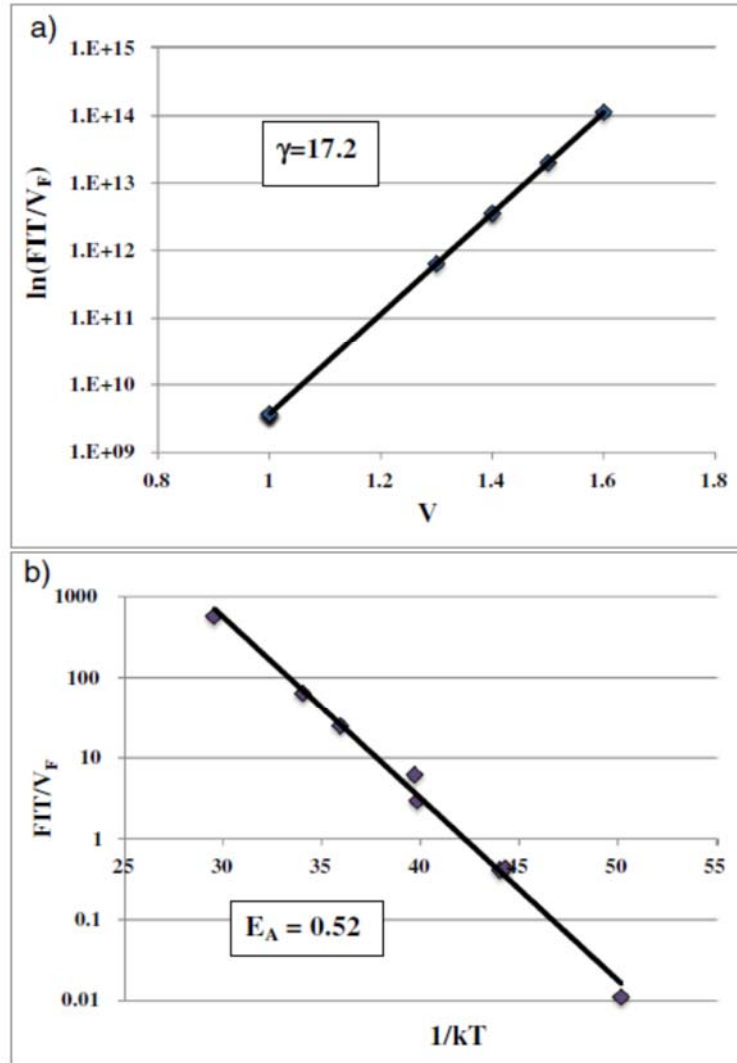
Figure 8 (a) Gamma plot for BTI at 28 nm, (b) Activation energy plot for BTI at 28 nm.

3.8 MTOL Matrix

Now that we have fully characterized the physics of failure models relating to all three mechanisms for both 45 and 28 nm FPGA's, we were able to build the Matrix Model by choosing three points, one from each mechanism, and then solve equations (1)–(3) against the measured FIT for each condition. In the 45 nm device experiments, we chose the following data shown in Table 2. The relative factors that solve the matrix are shown in Table 3.

Table 2 T, V, F and matrix versus measured FIT.

T °C	V	F(GHz)	HCI	BTI	EM	FIT
153	1.3	1	1.73E+6	6.73E-5	4.27E-15	3672
-35	2.5	0.5	4.7E+16	1.30E-07	8.96E-26	2.37E+7
154	1.2	0	0	6.96E-5	0	2420

Table 3 Relative weighting factors that solve the matrix.

HCI	5.03873E-10
BTI	34761994.46
EM	3.11618E+17

The procedure for finding the results of the matrix is described in previous papers [2,4,5]. This matrix has then used to construct the full reliability profile whereby FIT is calculated versus Temperature for several conditions, as shown in figure 9.
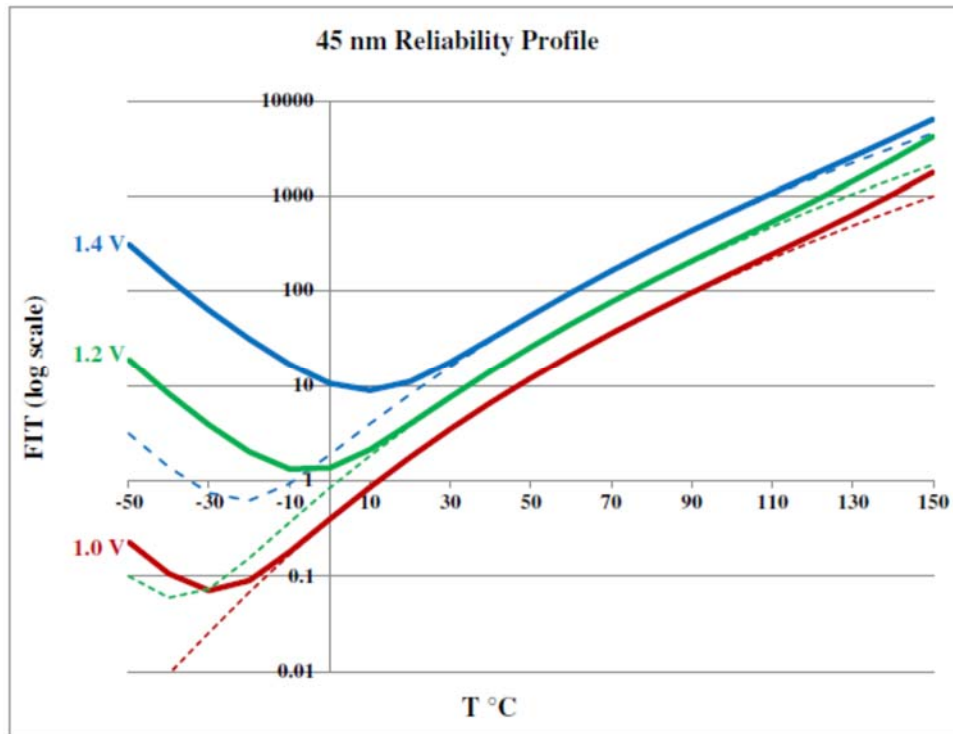
Figure 9 Reliability curves for 45 nm technology showing FIT versus Temperature for Voltages above and below nominal (1.2 V) and frequencies from 10 MHz (dashed line) to 2 GHz (solid line).

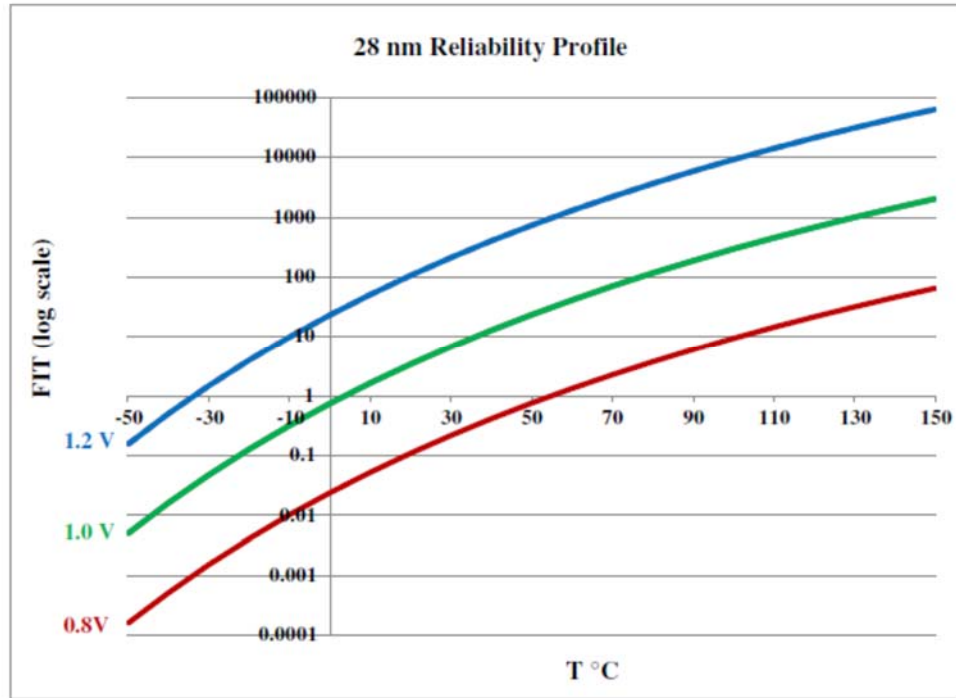The same curve has been made for the 28 nm technology node.

Figure 10 Reliability curves for 28 nm technology showing FIT versus Temperature for Voltages above and below nominal (1.0 V).

4   RESULTS AND DISCUSSION

The most notable differences between 45 and 28 nm is the lack of frequency effect at both low and high temperature, leaving only one, dominant, failure mechanism at 28 nm (Fig. 10). The consequence seems to be that there will be significantly improved reliability at low temperatures using 28 nm technology. Furthermore, there is no effect on frequency related to the reliability. Hence, there is no purpose for frequency derating using this technology. It is also clear that cooling the device is the major challenge and most important part of increasing the reliability of devices made using this technology [21]. Another observation is that the voltage acceleration is much greater at 28 nm, γ being over 17, as compared to 3.8

for 45 nm technology. This means that the core voltage is much more sensitive and a much greater reliability advantage would be gained by lowering the voltage. The temperature effect is exactly the same for both technologies.

One speculation as to the reason there are no hot carrier effects in the 28 nm technology is that the mean free path of electrons transported through the gate is larger than the gate length below a certain temperature. This would suggest that the electrons are transported by ballistic means below that temperature due to the properly strained channels. Hence, electrons are not able to accelerate to the point of causing damage due to HCI [22]. Data of normalized RO frequency (f/f_0), versus temperature supports this claim. The 28 nm devices have a distinct transition at a particular temperature (around 60 °C), whereas the 45 nm devices have not shown any transition along the entire range of temperatures. This observation will be expanded and reported in a later study. At higher temperatures, both 45 and 28 nm devices have similar slopes. This correlates with published data attributing the transistor channel conductance to the effect of "short channel ballistic conductance" at lower temperatures [23]. In order to validate the findings detailed above, the cause of this phenomenon is being further researched in our laboratory. We have yet to see if this is true for smaller technology, but it seems that this may be an important result justifying a preference to use newer scaled technology in high-reliability applications even over older technology that may seem more mature. Radiation and thermal cycles were not studied here and can also be subjects for future investigation.

5   CONCLUSIONS

In this research, an innovative and practical way to use the various physics of failure equations is shown together with accelerated testing for reliability prediction of devices exhibiting multiple failure mechanisms. Also presented was an integrated accelerating and measuring platform to be implemented inside FPGA chips, making the MTOL testing more accurate, allowing these tests at the chip and perhaps at

the system level, rather than only at the transistor level. The calibration of physics models with highly accelerated testing of complete commercial devices allows for actual reliability prediction. The MTOL Matrix can provide information about the proportional effect of each failure mechanism; allowing extrapolation of the expected reliability of the device under various conditions.

This practical platform can be implemented on almost any FPGA device and technology to enable making FIT calculations and reliability predictions. The results of this approach provide the basis for improvements in performance and reliability given any design or application. This method can be extended to other processes and new technologies, and can include more failure mechanisms, thus producing a more complete view of the system's reliability.

6   RECOMMENDATIONS

It is recommended that this work be extended to incorporate degradation mechanisms associated with radiation effects, including total ionizing dose effects, prompt ionizing dose effects, and charged particle (single event) effects, and into different technologies other than silicon CMOS such as GaN RF and other power devices. Additionally, it is recommended that the methodology be extended to incorporate it into a parts qualification procedure for space based systems since the method seems to accurately predict lifetime reliability.

REFERENCES

[1] "Xilinx, Device Reliability Report," UG116 (v10.3.1), Sept. 8 2015, https://www.xilinx.com/support/documentation/user_guides/ug116.pdf.

[2] J. Bernstein, Reliability Prediction from Burn-in Data Fit to Reliability Models, Elsevier Science and Technology Books, 2014.

[3] J.B. Bernstein, Physics-of-Failure Based Handbook of Microelectronic Systems, Reliability Information Analysis Center, Utica, NY, 2008.

[4] J.B. Bernstein, "Reliability Matrix Solution to Multiple Mechanism," *Microelectronics Reliability*, 54 (12), pp. 2951-2955, 2014.

[5] J. B. Bernstein, "Reliability Prediction for Aerospace Electronics," *IEEE Aerospace*, vol. 38, pp. 2042-2050, 1991.

[6] G. Groeseneken, "Hot Carrier Degradation," *Microelectron. Eng.,* pp. 27-40, 1999.

[7] X.Wang, "Impact of Interconnect Length on BTI and HCI Induced," *IEEE Reliability Physics Symposium J(IRPS),* 2012.

[8] C. Nunes, "BTI, HCI and TDDB Aging Impact in Flipflops," *Microelectron. Reliab. 53,* vol. 53, no. 9-11, pp. 1355-1359, 2013.

[9] J. Peng, "A Reliability Model for CMOS Circuit Based on Device Degradation," *IEEE Transactions on Electron Devices,* no. 978-1-4673-2475-5/12, pp. 1-3, 2012.

[10] J.B. Velamala, "Failure analysis of asymmetric aging," *IEEE Trans. Device Mater. Reliab.,* pp. 340-349, 2013.

[11] C. Liu, "Systematical Study of 14 nm FinFET Reliability: From Device Level," IEEE International Reliability Physics Symposium, Monterey, CA, 2015.

[12] JEDEC Solid State Technology Association, "Failure Mechanisms and Models for Semiconductor Devices," JEP-122G," Oct. 2011, http://www.jedec.org. (author not listed)

[13] G. Delarozee, "Introduction to Reliability," *Microelectron. Eng.,* vol. 49, pp. 3-10, 1999.

[14] M. A. H. Kufluoglu, "A Computational Model of NBTI and Hot Carrier Injection," *J. Comput. Electron.,* vol. 3, pp. 165-169, 2004.

[15] M.H. Hsieh, "The Impact and Implication of BTI/HCI Decoupling on Ring Oscillator," *Reliability Physics Symposium (IRPS), IEEE International*, Monterey, CA, 2015.

[16] S. Mahapatara, "Device scaling effects," *IEEE Trans. Electron Devices,* vol. 47, pp. 789-796, 2000.

[17] V. Huard, "NBTI Degradation: From Physical Mechanisms to Modeling," *Microelectron. Reliab.,* vol. 46, pp. 1-23, 2006.

[18] A. C. D. Young, "Failure Mechanism Models for Electromigration," *IEEE Trans. Reliab.,* vol. 43, pp. 186-192, 1994.

[19] M. Gall, "Statistical Analysis of Early Failures in Electromigration," *J. Appl. Phys.,* vol. 90, pp. 732-740, 2001.

[20] D.K. Schroder, "Negative Bias Temperature Instability: Road to Cross," *J. Appl. Phys.,* vol. 94, pp. 1-18, 2003.

[21] B. Tudor, "An Accurate MOSFET Aging Model," *Microelectron. Reliab.,* vol. 52, pp. 1565-1570, 2012.

[22] A. Acovic, "A Review of Hot-Carrier Degradation Mechanisms," *Microelectron. Reliab.,* vol. 36, pp. 845-869, 1996.

[23] V.K. Arora, "The Role of Ballistic Mobility and Saturation Velocity in Performance Evaluation of a Nano CMOS Circuit," International Conference on Emerging Trends in Electronic and Photonic Devices & Systems, Varanasi, India, 2009.

LIST OF ABBREVIATIONS, SYMBOLS AND ACRONYMS

AFOSR   Air Force Office of Scientific Research
AFOSR   Acceleration Factor
ASIA   Application Specific Integrated Circuits
BTI   Bias Temperature Instability
CMOS   Complementary Metal Oxide Semiconductor
EM   Electromigration
FIT   Failure in Time
FPGA   Field Programmable Gate Arrays
HCI   Hot Carrier Injection
HKMG   High-K Metal Gate
HTOL   High Temperature Operational Life
IR   Infrared
MTOL   Multiple Temperature Operational Life
MUX   Multiplexer
NBTI   Negative Bias Temperature Instability
PBTI   Positive Bias Temperature Instability
RO   Ring Oscillators
TDDB   Time Dependent Dielectric Breakdown
TIF   Time to Fail
TSMC   Taiwan Semiconductor Manufacturing Company

DISTRIBUTION LIST

DTIC/OCP
8725 John J. Kingman Rd, Suite 0944
Ft Belvoir, VA 22060-6218   1 cy

AFRL/RVIL
Kirtland AFB, NM 87117-5776   2 cys

Official Record Copy
AFRL/RVSW/Clay Mayberry   1 cy

(This page intentionally left blank)